

The emergence of the Star Formation Main Sequence with redshift unfolded by JWST

P. RINALDI,^{1,2} R. NAVARRO-CARRERA,¹ K. I. CAPUTI,^{1,3} E. IANI,¹ G. ÖSTLIN,⁴ L. COLINA,^{5,6} S. ALBERTS,²
J. ÁLVAREZ-MÁRQUEZ,⁵ M. ANNUNZIATELLA,⁵ L. BOOGAARD,⁷ L. COSTANTIN,⁵ J. HJORTH,⁸ D. LANGEROODI,⁸
J. MELINDER,⁴ T. MOUTARD,^{9,10} AND F. WALTER⁷

¹*Kapteyn Astronomical Institute, University of Groningen, P.O. Box 800, 9700AV Groningen, The Netherlands*

²*Steward Observatory, University of Arizona, 933 North Cherry Avenue, Tucson, AZ 85721, USA*

³*Cosmic Dawn Center (DAWN), Copenhagen, Denmark*

⁴*Department of Astronomy, Stockholm University, Oscar Klein Centre, AlbaNova University Centre, 106 91 Stockholm, Sweden*

⁵*Centro de Astrobiología (CAB), CSIC-INTA, Ctra. de Ajalvir km 4, Torrejón de Ardoz, E-28850, Madrid, Spain*

⁶*Cosmic Dawn Center (DAWN), Denmark*

⁷*Max-Planck-Institut für Astronomie, Königstuhl 17, 69117 Heidelberg, Germany*

⁸*DARK, Niels Bohr Institute, University of Copenhagen, Jagtvej 128, 2200 Copenhagen, Denmark*

⁹*Aix Marseille Univ, CNRS, CNES, LAM, Marseille, France*

¹⁰*European Space Agency (ESA), European Space Astronomy Centre (ESAC), Camino Bajo del Castillo s/n, 28692 Villanueva de la Canada, Madrid, Spain*

Submitted to ApJ

ABSTRACT

We investigate the correlation between stellar mass (M_*) and star formation rate (SFR) across the stellar mass range $\log_{10}(M_*/M_\odot) \approx 6 - 11$. We consider almost 50,000 star-forming galaxies at $z \approx 3 - 7$, leveraging data from COSMOS/SMUVS, JADES/GOODS-S, and MIDIS/XDF. This is the first study spanning such a wide M_* range without relying on gravitational lensing effects. We locate our galaxies on the SFR – M_* plane to assess how the location of galaxies in the star-formation main sequence (MS) and starburst (SB) region evolves with M_* and redshift. We find that the two star-forming modes tend to converge at $\log_{10}(M_*/M_\odot) < 7$, with all galaxies found in the SB mode. However, deeper observations will be instrumental for reaching lower SFRs and M_* to further validate this scenario. By dissecting our galaxy sample in M_* and redshift, we show that the emergence of the star-formation MS is M_* dependent: while in galaxies with $\log_{10}(M_*/M_\odot) > 9$ the MS is already well in place at $z = 5 - 7$, for galaxies with $\log_{10}(M_*/M_\odot) \approx 7 - 8$ it only becomes significant at $z < 4$. Overall, our results are in line with previous findings that the SB mode dominates amongst low stellar-mass galaxies. The earlier emergence of the MS for massive galaxies is consistent with galaxy downsizing.

Keywords: Galaxies: formation, evolution, high-redshift, star formation, starburst, Epoch of Reionization

1. INTRODUCTION

In recent decades, galaxy surveys up to very high redshifts have significantly advanced our understanding of galaxy evolution, constraining galaxy physical properties such as stellar mass (M_*) and star forma-

tion rates (SFR) (Le Floch et al. 2005; Ellis et al. 2013; Oesch et al. 2014; Bouwens et al. 2015; Stefanon et al. 2019; Bowler et al. 2020; Bhatawdekar & Conselice 2021; Bouwens et al. 2021). These quantities have been extensively used to constrain the process of gas conversion into stars, i.e., the stellar mass assembly (Casey et al. 2012; L’Huillier et al. 2012; Bauer et al. 2013; Jackson et al. 2020). Statistical analysis of extensive galaxy samples has established a correlation between M_* and SFR

in star-forming galaxies, revealing the “Main Sequence (MS) of star-forming galaxies”, and identified a passive cloud of galaxies with negligible star formation activity (Brinchmann et al. 2004; Noeske et al. 2007). These initial works triggered a vast amount of later papers studying galaxy evolution on the SFR – M_* plane (e.g., Peng et al. 2010; Speagle et al. 2014; Salmon et al. 2015; Santini et al. 2017).

The existence of a star formation main sequence indicates that similar mechanisms may drive the growth of both low- and high-mass galaxies (Noeske et al. 2007). The MS galaxies grow continuously over a long time period from smooth gas accretion (e.g., Sánchez Almeida et al. 2014). In particular, the position of a galaxy on the SFR – M_* plane has been proposed to be strictly correlated with its evolutionary stage (e.g., Tacchella et al. 2016), while the intrinsic scatter of the MS suggests some variety in the star formation histories (SFHs) for galaxies of a given stellar mass (e.g., Matthee & Schaye 2019).

Recent works have shown that the normalization of the SFR – M_* relation increases over cosmic time, particularly at $z \approx 0 - 3$, reflecting higher gas accretion rate and, therefore, higher SFR in the past (e.g., Whitaker et al. 2012, 2014; Iyer et al. 2018; Popesso et al. 2023). Usually, this relation is modeled as a power-law, $\log_{10}(\text{SFR}) = \alpha \log_{10}(M_*) + \beta$ (see Speagle et al. 2014 for a more detailed study).

In addition, other works have analyzed the presence of galaxies with significantly enhanced star formation activity at high redshifts, the so-called *starbursts* (SB), on the SFR – M_* plane. However, to date, there is no absolute consensus in the literature on the definition of a starburst. Some studies simply consider that SB galaxies are those sources with a very high SFR (order of $10 - 100 M_\odot \text{yr}^{-1}$; see Muxlow et al. 2006; Heckman 2006) and, therefore, they are located several σ above the MS, where σ refers to the observed scatter of the MS relation (e.g., Elbaz et al. 2011; Rodighiero et al. 2011; Schreiber et al. 2015; Lee et al. 2017; Orlitova 2020). One could adopt instead a criterion more in line with the textbook definition of starburst (Heckman 2006), which refers to the galaxy birthrate parameter: a galaxy is in a SB episode when its ongoing SFR is much higher than its average past SFR. However, constraining the average past SFR of a galaxy is not trivial, as it assumes knowing its star formation history and age.

More recently, an alternative definition of starbursts for high-redshift galaxies has been empirically proposed: starbursts are galaxies with high specific star formation rates (sSFRs), with $\log_{10}(\text{sSFR}/\text{yr}^{-1}) > -7.60$ (Caputi et al. 2017, 2021). The inverse of the sSFR

represents the stellar mass doubling time, with the above limit corresponding to values $< 4 \times 10^7$ yr. This is comparable to the short star formation timescales ($10^6 - 10^7$ yr) observed in local starburst regions (e.g., Leitherer 2001). Additionally, these star formation timescales are consistent with the upper limits set by gas depletion time scales (10^8 yr) observed in local starburst galaxies, where intense star formation rapidly converts the available gas into stars (e.g., Mihos & Hernquist 1994; Knapen & James 2009).

In any case, the origin of the SB phenomenon is not completely understood. Current theories propose that starbursts may be driven by large-scale gravitational instabilities, which are influenced by stellar self-gravity (Inoue et al. 2016; Romeo & Fathi 2016; Tadaki et al. 2018). Alternatively, starbursts might result from multiple star formation bursts, often triggered by galaxy mergers (Lamastra et al. 2013; Calabrò et al. 2019).

Earlier assessments that SB galaxies played a minor role in cosmic star-formation history were based on data from relatively massive galaxies with $M_* \gtrsim 10^{10} M_\odot$ up to $z \approx 2$ (Rodighiero et al. 2011; Sargent et al. 2012; Lamastra et al. 2013). However, this view has now been reconsidered following the advent of deeper datasets that allow for the study of less massive galaxies.

In this regard, Caputi et al. (2017), by studying a sample of galaxies with $M_* \gtrsim 10^9 M_\odot$ at $z \approx 4 - 5$, discovered a significant fraction of SB and found that star-forming galaxies displayed a bimodal distribution (SB/MS) on the SFR- M_* plane. Later on, Bisigello et al. (2018) analyzed a deep sample of star-forming galaxies at $z \approx 0 - 3$ and determined that the fraction of SB galaxies increases both with redshift and towards lower stellar masses. Building on these findings, Rinaldi et al. (2022) further confirmed the existence of the SB/MS bimodality across a wider range of redshifts ($z \approx 3 - 6.5$), showing that this bimodality does not depend on the adopted SFR tracer (e.g., UV or $\text{H}\alpha$). These previous studies indicate that the SB population is much more significant than previously thought, underscoring the importance of studying low-mass galaxies to fully unveil the role of SBs in galaxy evolution.

In this study we make use of ultra-deep JWST data to extend the study of the star-forming galaxy distribution on the SFR – M_* plane down to very low stellar masses. We complement our analysis with the Spitzer Matching survey of the Ultra-VISTA ultra-deep stripes (SMUVS; Ashby et al. 2018) catalog to trace the high-mass end of the SFR- M_* plane, allowing us to cover in total five decades in stellar mass ($\log_{10}(M_*/M_\odot) \approx 6 - 11$). Our main goal is to understand when the star-formation MS

appeared in cosmic time for galaxies of different stellar masses.

The structure of the paper is as follows. Section 2 provides an overview of our sample, comprising over 50,000 star-forming galaxies, and Section 3 details our methodology. In Section 4, we present our findings. Specifically, in Section 4.2, we show the SFR – M_* plane across four redshift bins: $z \approx 2.8–3.2$, $z \approx 3.2–3.9$, $z \approx 3.9–5$, and $z \approx 5–7$ and validate the SB/MS bimodality at these cosmic epochs. Subsequently, we analyze the sSFR distribution. In Section 4.3, we study the emergence of the MS as a function of stellar mass. Finally, in Section 4.4, we analyze the emergence of the MS as a function of both cosmic time and stellar mass. Section 5 summarizes our key findings.

Throughout this paper, we consider a cosmology with $H_0 = 70 \text{ km s}^{-1} \text{ Mpc}^{-1}$, $\Omega_M = 0.3$, and $\Omega_\Lambda = 0.7$. All magnitudes are total and refer to the AB system (Oke & Gunn 1983). A Chabrier (2003) initial mass function (IMF) is assumed (0.1–100 M_\odot). We define SB as galaxies with $\text{sSFR} > 10^{-7.60} \text{ yr}^{-1}$ (Caputi et al. 2017, 2021).

2. DATASET

In this work, we made use of data from two fields: the JWST Advanced Deep Extragalactic Survey (JADES) in the GOODS-South (GOODS-S) region (67.7 arcmin²) and the COSMOS/SMUVS survey (0.66 deg²).

2.1. JADES/GOODS-S

For this field, we considered the complete dataset from JADES/GOODS-S data release 2 (DR2), covering a total of 67.7 arcmin². This dataset encompasses the Hubble eXtreme Deep Field (XDF; Koekemoer et al. 2013), which includes ultra-deep MIRI data at 5.6 μm from MIRI Deep Imaging Survey (MIDIS; Östlin et al. 2024, in prep.). We summarize filters and depths in Table 1.

2.1.1. MIRI data

In this work, we made use of the MIDIS/F560W ultra-deep observations carried out in December 2022 over Hubble XDF. These data will be described in Östlin et al. (2024) and consist of ≈ 40 hours on source taken in the HUDF, which allowed us to reach 28.6 mag (5σ) for point-like sources measured in an $r=0''.23$ circular aperture (the radius being chosen to ensure a $\approx 70\%$ encircled energy). For a more comprehensive view on the MIRI data reduction, refer to Section 2.1.2 in Rinaldi et al. (2023). However, only a small fraction of the sources in GOODS-S has a detection in F560W from MIDIS at $z \approx 3–7$ ($\lesssim 2\%$). More in general, MIRI plays a minimal role in this study because NIRCcam alone,

Table 1. 5σ Photometric Depth in JADES/GOODS-S

Instrument	Filter	Depth (nJy)
		JADES Deep & Medium
HST/ACS	F435W	2.33 / 10.77
HST/ACS	F606W	3.61 / 6.96
HST/ACS	F775W	2.22 / 15.79
HST/ACS	F814W	8.20 / 7.2
HST/ACS	F850LP	4.28 / 17.53
JWST/NIRCcam	F090W	3.55 / 6.26
JWST/NIRCcam	F115W	2.93 / 5.44
JWST/NIRCcam	F150W	2.89 / 5.53
JWST/NIRCcam	F182M	8.04 / 9.53
JWST/NIRCcam	F200W	3.01 / 5.27
JWST/NIRCcam	F210M	5.83 / 12.11
JWST/NIRCcam	F277W	2.17 / 4.24
JWST/NIRCcam	F335M	3.64 / 3.81
JWST/NIRCcam	F356W	2.46 / 4.07
JWST/NIRCcam	F410M	3.23 / 6.43
JWST/NIRCcam	F430M	7.84 / 7.31
JWST/NIRCcam	F444W	2.79 / 5.11
JWST/NIRCcam	F460M	10.71 / 9.61
JWST/NIRCcam	F480M	7.98 / 6.51
JWST/MIRI	F560W	13.18

NOTE—Table adapted from Hainline et al. (2024). Fluxes are in nJy and measured within an aperture of $r = 0.2''$. JADES Deep and Medium values are separated by a slash (see Figure 3 in Hainline et al. 2024). We do not report HST/UVIS (F225W, F275W, and F336W). MIRI/F560W refers to XDF only and its depth was measured in an aperture of $r = 0.23''$.

given the redshift range probed ($z \approx 3–7$), traces the rest-frame spectra of nearly 99% of our sample beyond H α (up to $z \approx 6.5$), ensuring robust estimates of stellar properties (e.g., M_*). Indeed, it has been shown in the literature that MIRI detections, when combined with sufficient data from HST and NIRCcam (i.e., our worst-case scenario ensures at least 13 bands without MIRI), do not significantly impact the estimation of stellar properties through spectral energy distribution (SED) fitting (see, e.g., Boogaard et al. 2023; Alberts et al. 2024; Iani et al. 2024; Li et al. 2024; Lyu et al. 2024).

2.1.2. NIRCcam data

We also considered the NIRCcam imaging taken by the JWST Advanced Deep Extragalactic Survey, JADES (Eisenstein et al. 2023a), Data Release 2 (DR2; Eisenstein et al. 2023b), which includes observations from the JWST Extragalactic Medium-band Survey (JEMS;

Williams et al. 2023) and the First Reionization Epoch Spectroscopically Complete Observations (FRESCO, Oesch et al. 2023). This dataset provides a total of 14 bands from 0.9 to 4.8 μm (6 at short-wavelength, SW, and 8 at long-wavelength, LW), with 5σ depths ranging from 30.5 to 30.9 mag (measured in a $0.2''$ radius circular aperture). We remark that JADES is one of the deepest NIRCcam surveys on the sky, only matched in depth (in some bands) by the MIDIS/NIRCcam-parallel project (Pérez-González et al. 2023) and The Next Generation Deep Extragalactic Exploratory Public Near-Infrared Slitless Survey, NGDEEP (Bagley et al. 2024), which means that we can have access to very low-mass galaxies that, prior JWST’s launch, were accessible only thanks to lensed fields (e.g., Santini et al. 2017; Rinaldi et al. 2022).

2.1.3. HST data

We obtained all the HST images over GOODS-S from the Hubble Legacy Field (HLF/GOODS-S). The HLF/GOODS-S provides 13 HST bands covering a wide range of wavelengths (0.2–1.6 μm), from the UV (WFC3/UVIS F225W, F275W, and F336W filters), optical (ACS/WFC F435W, F606W, F775W, F814W, and F850LP filters), to near-infrared (WFC3/IR F098M, F105W, F125W, F140W and F160W filters). In this work, we only made use of the deepest ones (i.e., F435W, F606W, F775W, F814W, F850LP, F105W, F125W, F140W, F160W). We refer the reader to Whitaker et al. (2019) for a more detailed description of these observations¹.

2.2. COSMOS/SMUVS

As a complement, we leverage the SMUVS catalog compiled by Deshmukh et al. (2018) and later updated by van Mierlo et al. (2022), encompassing $\approx 300,000$ *Spitzer* sources with 28-band photometry from *U* band to 4.5 μm .

Briefly, SMUVS utilized *Spitzer*’s IRAC at 3.6 and 4.5 μm across 0.66 deg² of the COSMOS field (Scoville et al. 2007), integrating ≈ 25 h/pointing and achieving 80% completeness at ≈ 25.5 mag (Deshmukh et al. 2018). This survey overlaps with the deepest near-IR and optical data from UltraVISTA (McCracken et al. 2012) and Subaru (Taniguchi et al. 2007), respectively.

The catalog adopted in this work is based on the ultra-deep UltraVISTA HKs stacked image (Deshmukh et al. 2018). The SED fitting was performed using LEPHARE, utilizing synthetic templates from Bruzual &

Charlot (2003) and a reddening law by Calzetti et al. (2000), as detailed in Deshmukh et al. (2018). In particular, we focused only on star-forming galaxies at $z \approx 3 - 7$.

By design, SMUVS enables the exploration of a very different region of the parameter space in the SFR – M_* plane, as it spans an area approximately $35\times$ larger than that covered by JADES in GOODS-S (although it is about three magnitudes shallower). This makes SMUVS particularly effective for probing the high-mass end, which smaller fields cannot adequately sample.

3. PHOTOMETRY AND SED FITTING

In this section, we provide an overview of the photometry and SED fitting performed for our sources in JADES/GOODS-S. A comprehensive explanation of the photometry and SED fitting for sources in JADES/GOODS-S is presented in Navarro-Carrera et al. (2024a). For the SMUVS sources, detailed methodologies are referenced in Deshmukh et al. (2018) and van Mierlo et al. (2022).

3.1. Photometry

We adopted SEXTRACTOR (Bertin & Arnouts 1996) to perform the source detection and extract the photometry across all HST and JWST images (with a pixel scale of 30 mas for both HST and NIRCcam images and 60 mas for MIRI/F560W). We adopted a detection strategy similar to the one adopted in Rinaldi et al. (2023, 2024) and Navarro-Carrera et al. (2024b). The detection has been performed by using a super stack image combining F277W, F335M, F356W, F410M, and F444W.

We used SEXTRACTOR by considering a hot-mode configuration, following Galametz et al. (2013) which has been proved being well suited for detecting very faint sources. Particularly, we adopted a detection threshold of 2σ and a minimum number of contiguous pixels of 9.

We recovered more than 85% of the JADES DR2 official catalog. Interestingly, when anti-crossmatching with the official JADES DR2 catalog (Eisenstein et al. 2023b), we found a substantial number of real sources (visually inspected) which have not been reported in the official JADES DR2 catalog (due to the different detection and deblending strategies, especially close to very bright and extended sources).

We built up our photometric catalog following the same approach as the one adopted in Rinaldi et al. (2023, 2024) and Navarro-Carrera et al. (2024b). Briefly, we combined aperture-corrected photometry, adopting circular apertures (i.e., MAG_APER) of $0.5''$ diameter, and Kron apertures (i.e., MAG_AUTO – Kron 1980). We chose a circular-aperture flux over a Kron flux when the sources

¹ The HLF/GOODS-S imaging is available at <https://archive.stsci.edu/prepds/hlf/>;

were fainter than a given magnitude. In this case, as we were dealing with very deep images, we adopted $\text{mag}_{\text{lim}} = 27$ as our faint limit for the Kron aperture. The aperture correction for JWST images has been obtained by using the software WEBBPSF (Perrin et al. 2014). When SEXTRACTOR, for a given source, was not able to recover any flux, we estimated an upper limit (3σ): we placed random apertures ($0.25''$ radius) in a square box ($20'' \times 20''$) around each source and measured the local background, assigning -1 as an error. For those sources, instead, with no photometric coverage, we simply put -99 . All fluxes have been corrected for Galactic extinction by using DUSTMAPS (Green 2018). Finally, for each source, we imposed a minimum error of 0.05 mag to account for photometric calibration uncertainties and error underestimation by SEXTRACTOR (Sonnott et al. 2013).

We double-checked our photometry with the one from the official JADES DR2 catalog and found good agreement. See Navarro-Carrera et al. (2024a) for more details.

3.2. SED fitting

Once we built up our photometric catalog, we performed SED fitting for all our sources. We adopted a two-step process. We first derived photometric redshifts by using EAZY (Brammer et al. 2008) and, then, derived the stellar properties with LEFHARE (Arnouts & Ilbert 2011). This guarantees that the same SED fitting code to derive stellar properties was used for both samples (JADES/GOODS-S and SMUVS), ensuring consistency in the derived results.

The EAZY SED fitting has been performed by adopting a linear combination of different templates. Particularly, we adopted the same templates as the ones used in Eisenstein et al. (2023b); Hainline et al. (2024). This approach allowed us to reach an outlier fraction of $\approx 8\%$ (see Figure 1, already presented in Navarro-Carrera et al. 2024a), considering a large amount of spectroscopic redshifts (> 1000) in GOODS-S from different programs (e.g., JADES/NIRSpec MSA, 3D-HST, MUSE, and CANDELS/GOODS-S; Brammer et al. 2012; Guo et al. 2013; Bacon et al. 2023; Bunker et al. 2023).

Once we derived the photometric redshifts from EAZY and established the goodness of our results, we inferred the stellar properties of our sources with LEFHARE by fixing the redshifts to the photometric estimate by EAZY and adopting the same approach as the one used in Rinaldi et al. (2023, 2024). Briefly, we considered the stellar population synthesis (SPS) models proposed by Bruzual & Charlot (2003), based on the Chabrier

IMF (Chabrier 2003). We made use of two different star formation histories (SFHs): a standard exponentially declining SFH (known as “ τ -model”) and an instantaneous burst adopting a simple stellar population (SSP) model. We opted for two distinct metallicity values, a solar metallicity ($Z_{\odot} = 0.02$) and a fifth of solar metallicity ($Z = 0.2Z_{\odot} = 0.004$). We considered the Calzetti et al. (2000) reddening law in combination with Leitherer et al. (2002). In particular, we adopted the following color excess values: $0 \leq E(B - V) \leq 1.5$, with a step of 0.1 mag. **This setup is very similar to the one used by Deshmukh et al. (2018) and van Mierlo et al. (2022) for the SMUVS catalog.** When a spectroscopic redshift was available, we fixed it to the spectroscopic value rather than the photometric redshift estimated by EAZY.

A more detailed description of the adopted methodology for the SED fitting is presented in Navarro-Carrera et al. (2024a).

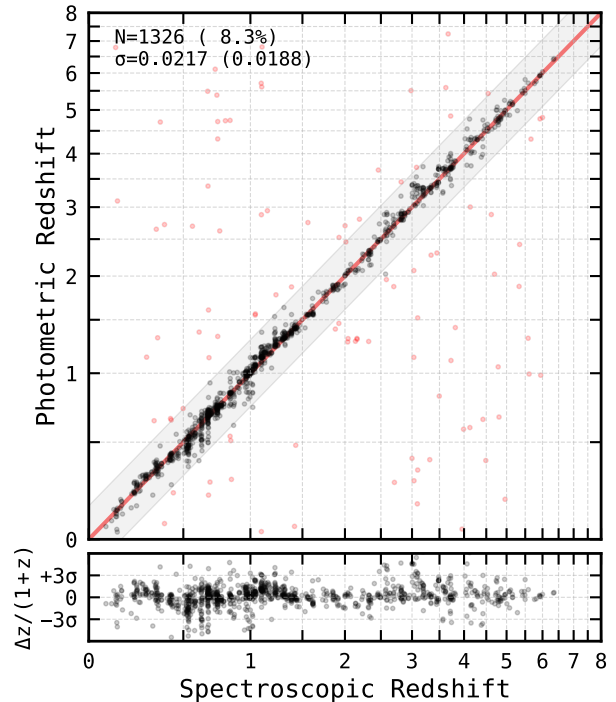


Figure 1. Comparison between spectroscopic and photometric redshifts in JADES/GOODS-S from Navarro-Carrera et al. (2024a).

4. RESULTS

We considered our independent determinations of M_{\star} (from SED fitting) and SFRs (from rest-frame UV dust-corrected luminosities) to locate our sample of galaxies (JADES/GOODS-S) on the SFR– M_{\star} plane at $z \approx 3-7$

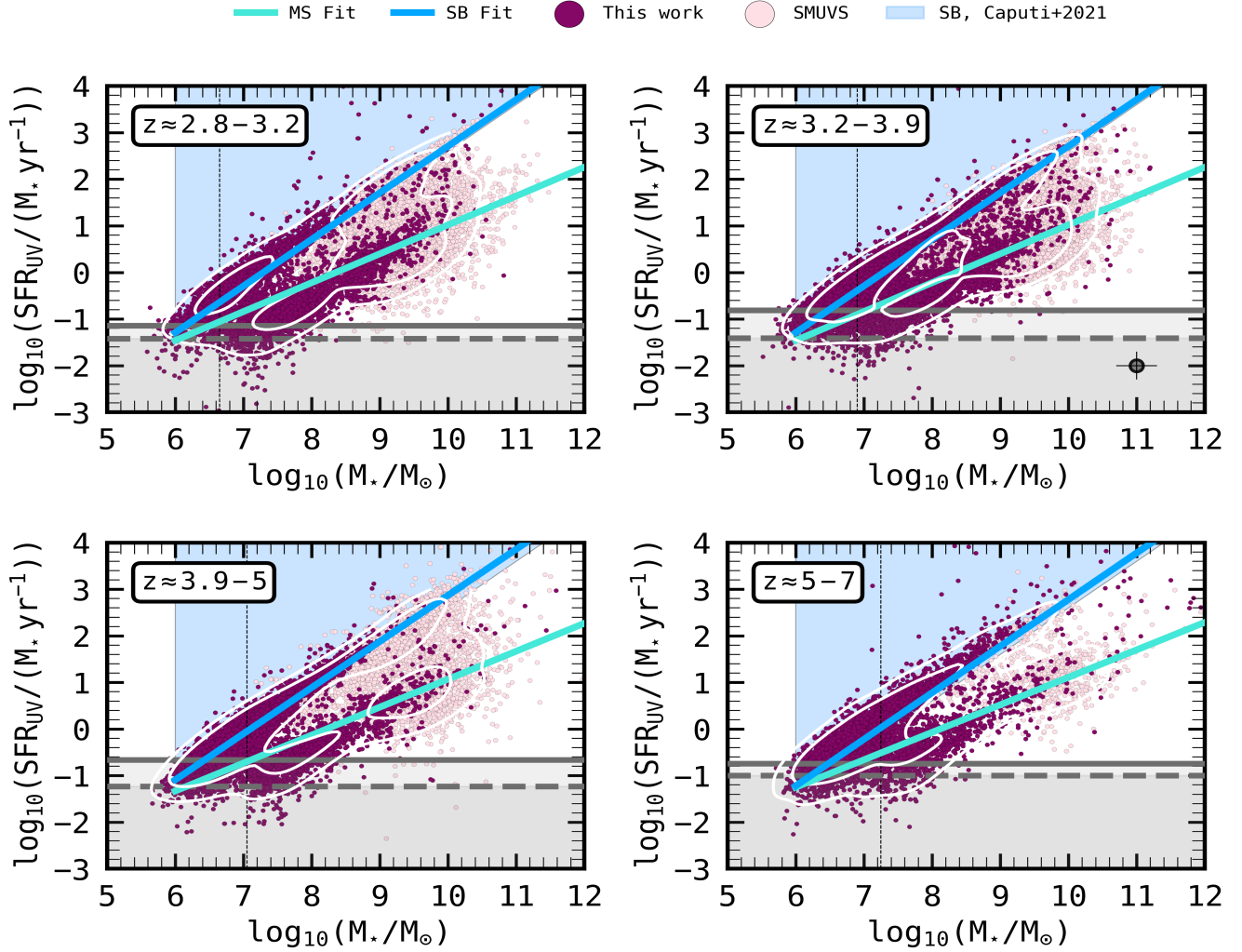


Figure 2. The SFR – M_* plane, showcasing all sources (JADES/GOODS-S + COSMOS/SMUVS) analyzed in this study, divided in redshift bins as indicated. The pale blue region marks the lower envelope for SB galaxies, based on the criteria from Caputi et al. (2017, 2021). Fits for the MS and SB are derived from Rinaldi et al. (2022). The vertical dashed line in each panel refers to the stellar mass completeness (75%) of JADES sample at each redshift. The error bar showed in gray (upper right panel) indicate the median uncertainties on M_* and SFR. White contours (68% and 95%) are also presented to show the bimodality between MS and SB. The gray horizontal lines indicate the SFR threshold derived from the 3σ limiting flux of the band used to estimate the rest-frame 1500 \AA . Specifically, when two different filters were used to probe this wavelength for a given redshift bin (e.g., HST/F775W and NIRCcam/F090W for $z \approx 3.9 - 5$), we adopted the average 3σ limiting flux. The dashed lines correspond to JADES/Deep, while the solid lines represent JADES/Medium (see Table 1).

complemented with the one from COSMOS/SMUVS, as shown in Figure 2. Additionally, we investigated the sSFR distribution of these galaxies, illustrated in Figure 3 and Figure 4. Finally, we inspected the evolution of the MS and SB percentages as a function of redshift at different stellar mass regimes (Figure 5). Our results do not change if SFRs from best-fit SEDs are adopted as SFRs derived from the best-fit models are similarly influenced by dust corrections, as they also rely on the modeled rest-frame UV luminosity.

4.1. Star Formation Rate estimates from the UV

We derived the SFRs for our sample independently of their SED fitting by considering their rest-frame UV luminosities (L_ν). To do so, we estimated L_ν at a reference wavelength $\lambda_{rest} = 1500 \text{ \AA}$ from the photometry of every galaxy at the filter with the closest effective wavelength to $\lambda_{obs} = \lambda_{rest} \times (1+z)$, where z is the photometric redshift of that galaxy. We corrected the UV fluxes for dust extinction following the Calzetti et al. (2000) reddening law in order to recover the intrinsic UV fluxes. In order to do so, we adopted $E(B-V)$ values from the SED fitting analysis. Then we converted them into a monochromatic luminosity (L_ν). Finally we

obtained SFR_{UV} using the prescription given by Kennicutt (1998):

$$\text{SFR}(M_{\odot} \text{ yr}^{-1}) = 1.4 \times 10^{-28} L_{\nu}(\text{erg s}^{-1}\text{Hz}^{-1}). \quad (1)$$

The conversion formula (Eq. 1) has an intrinsic scatter of 0.3 dex. Therefore, we propagated that error into our uncertainty on the SFR. Furthermore, Eq. 1 is based on a Salpeter IMF (Salpeter 1955), while, in this work, we used a Chabrier one. Therefore, we scaled our SFRs from a Salpeter IMF to a Chabrier by considering a conversion factor (i.e., 1.55 as reported in Madau & Dickinson 2014).

4.2. The bimodality between MS and SB galaxies

Over recent decades, numerous studies have identified that star-forming galaxies predominantly lie along the so-called ‘‘Main-Sequence of star-forming galaxies’’ (Brinchmann et al. 2004; Elbaz et al. 2007; Speagle et al. 2014; Whitaker et al. 2014; Salmon et al. 2015). Only a subset of these sources was classified as starburst galaxies, ranging from about 2% (Rodighiero et al. 2011) to about 30% (Caputi et al. 2017), depending on the stellar mass cut.

However, these prior studies were limited by their observational depth. In this work, we leveraged deep observations from HST and JWST in GOODS-S, with the latter reaching 5σ depth of about 30.5 mag (Eisenstein et al. 2023b; Hainline et al. 2024). These ultra-deep observations enabled us, for the first time, to explore a region of the parameter space that, previously, was only accessible through the study of lensed fields (i.e., by exploiting the gravitational lensing effect). The latter, prior JWST’s launch, was the only way to probe very low-mass galaxies (e.g., Santini et al. 2017; Atek et al. 2018; Bhatawdekar & Conselice 2021; Rinaldi et al. 2022). Notably, in this study, we expanded our dataset with data from SMUVS (Deshmukh et al. 2018), which allowed us to extend our study toward the high-mass end of the $\text{SFR} - M_{\star}$ plane. Overall, our statistical sample consists of more than $\approx 50,000$ galaxies, giving us the opportunity, for the first time, to study the $\text{SFR} - M_{\star}$ plane over five decades in stellar mass across cosmic time ($z \approx 3 - 7$) in blank fields.

Following the criteria established in Caputi et al. (2017, 2021), our analysis reveals that approximately 41% of the galaxies in our sample is located along the MS (i.e., they have $\log_{10}(\text{sSFR}/\text{yr}^{-1}) < -8.05$), while about 48% of the sources is placed within the SB cloud (i.e., they have $\log_{10}(\text{sSFR}/\text{yr}^{-1}) > -7.60$). The residual 11% of our sample is located in the so-called ‘‘Star Formation Valley’’ (SFV). The SFV region in the $\text{SFR} - M_{\star}$ plane is indicative of galaxies either transitioning from

the MS to SB, experiencing a rejuvenation effect (Rosani et al. 2020; Zhang et al. 2023), or moving from SB back to MS, thereby returning to a steady state after a burst of intense star formation, probably triggered by disk instabilities or (minor and/or major) mergers.

Interestingly, when we apply the same mass cut ($\log_{10}(M_{\star}/M_{\odot}) \gtrsim 10$) to galaxies as used by Rodighiero et al. (2011), we find that SB galaxies constitute only 2% at $z \gtrsim 2.8$. This is in agreement with the findings reported by Rodighiero et al. (2011) at $z \approx 2$, regardless of which sSFR cut is adopted.

All in all, this comparison suggests that focusing solely on massive galaxies (i.e., $\log_{10}(M_{\star}/M_{\odot}) \gtrsim 10$) might lead to a significant underestimation of the role of SB galaxies in the Cosmic Star Formation History, since the starburst phase in high mass galaxies is typically triggered by significant events such as major mergers, as highlighted by studies like Pearson et al. (2019) and Renaud et al. (2022).

Notably, so far, the SB cloud has been defined only down to $\log_{10}(M_{\star}/M_{\odot}) \approx 9$ (Caputi et al. 2017, 2021). In Figure 2, we report an extrapolation toward lower stellar masses ($\log_{10}(M_{\star}/M_{\odot}) = 6$) of the SB lower envelope (pale blue shade). Interestingly, from Figure 2, we can observe that this extrapolation nicely follows the separation in two clouds between MS and SB galaxies. Indeed, one should note that this SB lower envelope corresponds to the M_{\star} doubling time of approximately 4×10^7 yr, aligning with the typical timescales of local SB episodes as proposed in Knappen & James (2009). Therefore, classifying all galaxies with $\log_{10}(\text{sSFR}/\text{yr}^{-1}) > -7.60$ as SB galaxies is consistent across all M_{\star} ranges, as demonstrated in Figure 2.

We then divided our galaxy sample into four distinct redshift bins, following the same approach as the one used in Rinaldi et al. (2022). Specifically, 27% of our sample is located within the redshift range $z \approx 2.8 - 3.2$, 32% falls in the $z \approx 3.2 - 3.9$ range, 24% are in the $z \approx 3.9 - 5$ interval, and the remaining 17% is located within $z \approx 5 - 7$ range. The above division in redshift bins has been adopted in order to probe the same amount of time (≈ 400 Myr) in each redshift bin. Notably, we retrieve the bimodality between MS and SB in each redshift bin. This finding further supports the existence of this bimodality, as previously suggested in Caputi et al. (2017, 2021); Rinaldi et al. (2022).

As a sanity check, we also inspected all sources in our sample that show a photometric excess ascribable to the $\text{H}\alpha$ emission line by using the same approach as the one adopted in Rinaldi et al. (2023); Caputi et al. (2024). We first estimated their SFRs($\text{H}\alpha$) and, then, their corresponding sSFR($\text{H}\alpha$). Finally, we looked at the sSFR

distribution, confirming that the SB/MS bimodality is evident and does not depend on which SFR is adopted, as already shown in Rinaldi et al. (2022). A complete analysis of the H α emission of those sources is presented in Navarro-Carrera et al. (2024a).

Finally, in Figure 2, we note the presence of gray horizontal lines representing the 3σ limiting fluxes of the bands used to estimate SFR $_{UV}$. Specifically, the dashed lines correspond to the JADES/Deep region of GOODS-S, while the solid lines represent JADES/Medium (see Figure 3 in Hainline et al. 2024). Notably, with some scatter, our sample consistently lies above the SFR $_{UV}$ threshold achievable in the JADES/Deep region of GOODS-S across all redshift bins analyzed in this study. The vertical dashed line indicates the M_* completeness limit, corresponding to 75% completeness.

Interestingly, below $\log_{10}(M_*/M_\odot) < 7$, there is no clear distinction between MS and SB galaxies; instead, galaxies appear to mostly populate the SB cloud. This trend could be explained either by an increased burstiness of star formation that becomes important as we progressively go to lower stellar masses (Atek et al. 2022; Navarro-Carrera et al. 2024a), or by the current limitations in observational depth. Future deeper observations will be instrumental to explore lower SFRs and M_* to further validate this finding.

4.3. The emergence of the MS across the stellar mass range

Since our sample spans five decades in M_* within the SFR – M_* plane, we investigated the evolution of the SB/MS bimodality as a function of M_* to identify whether there is a specific stellar mass regime where the “Main Sequence of star-forming galaxies” takes place.

We divided our sample into the following stellar mass bins: $\log_{10}(M_*/M_\odot) \leq 7$, $\log_{10}(M_*/M_\odot) \approx 7 - 8$, $\log_{10}(M_*/M_\odot) \approx 8 - 9$, and $\log_{10}(M_*/M_\odot) > 9$.

Specifically, we analyzed the sSFR distribution within each stellar mass bin. To address the significant differences in survey area between our datasets, we normalized the JADES/GOODS-S (67.7 arcmin 2) counts to match the COSMOS/SMUVS survey area (0.66 deg 2), which is approximately 35 times larger than that covered by JADES/GOODS-S.

From Figure 3, we note that in the lowest mass regime ($\log_{10}(M_*/M_\odot) \leq 7$), MS galaxies are almost absent, constituting less than 3% of the total population at those stellar masses. Interestingly, we find the same result when looking at the sample of H α -emitters at $z \gtrsim 2.8$ (Navarro-Carrera et al. 2024a). By looking at their stel-

lar ages² (as indicated by the color bar on the right in Figure 3), we note that MS galaxies, albeit rare, preferentially show an older population compared to the starbursts in the same stellar mass bin. This suggests that MS galaxies may have already reached a steady state (e.g., Wang et al. 2019), with no significant feedback mechanisms triggering new star formation episodes (e.g., Renaud et al. 2019) and, therefore, young and massive stars are not entirely dominating their light.

Lastly, by looking at the HAEs that fall in this stellar mass regime, we find that galaxies show a very high H α equivalent width (EW) and are preferentially located in the starburst cloud, which confirms that these sources are going through a violent episode of star formation. On the contrary, the low-mass HAEs that show a low EW(H α) preferentially lie along the MS and represent a very minor fraction of the entire population of HAEs ($\lesssim 1\%$) (Navarro-Carrera et al. 2024a).

However, we caution the reader that the fact that galaxies preferentially appear to be in a SB phase at lower stellar masses ($\log_{10}(M_*/M_\odot) \leq 7$) could be explained either by an increase in the burstiness of star formation, which becomes more significant as M_* decreases (Atek et al. 2022; Navarro-Carrera et al. 2024a), or by the limitations of current observational depth which prevent us to detect low-stellar mass objects along the MS. Deeper observations will be crucial to shed light on this result.

Moving to higher stellar mass bins, MS galaxies (i.e., those sources with $\log_{10}(\text{sSFR}/\text{yr}) < -8.05$) begin to emerge marking the onset of the “Main Sequence of star-forming galaxies”, as we observe for galaxies with stellar mass $\log_{10}(M_*/M_\odot) \approx 7 - 8$, and the SB/MS bimodality becomes more prominent, especially at $\log_{10}(M_*/M_\odot) \approx 8 - 9$.

As we move to the highest stellar mass bin ($M_* \gtrsim 10^9 M_\odot$), MS galaxies dominate the entire sample, now accounting for approximately 64% at those stellar masses, which favours the picture pointed out in Rodighiero et al. (2011) where SB galaxies become increasingly rare as we move toward higher M_* (especially at $\log_{10}(M_*/M_\odot) \gtrsim 10$). On the other hand, the HAEs that fall in this stellar mass regime are characterized by having a very low EW(H α), due to the strong anticorrelation between M_* and EW(H α) (already pointed out in Atek et al. 2022 and further demonstrated in Navarro-Carrera et al. 2024a), indicating a lack of in-

² The ages for our galaxies directly come from LEPHARE and they are purely based on the formation time as given by Bruzual & Charlot (2003) models (i.e., the models that we used to perform the SED fitting);

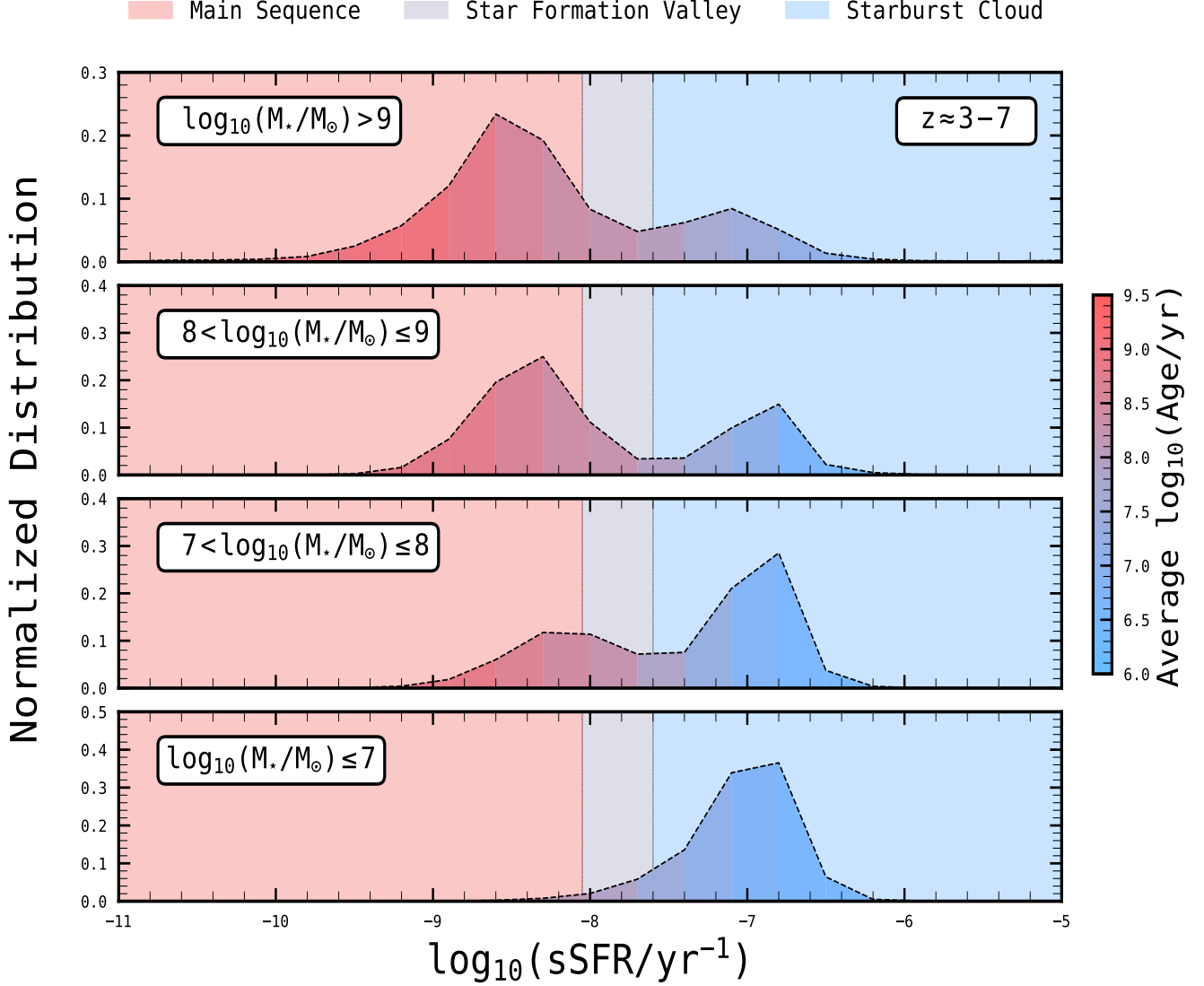


Figure 3. The sSFR distribution of the entire sample (JADES/GOODS-S + COSMOS/SMUVS) divided in four distinct stellar mass bins. The entire plane is colour coded following the regions derived by Caputi et al. (2017): the star-formation MS for $\text{sSFR} > 10^{-8.05} \text{ yr}^{-1}$, the Starburst cloud for $\text{sSFR} > 10^{-7.60} \text{ yr}^{-1}$, and the Star Formation Valley for $10^{-8.05} \text{ yr}^{-1} \leq \text{sSFR} \leq 10^{-7.60} \text{ yr}^{-1}$. The sSFR distribution are color coded by age, as derived by LEPHARE. To consider the different areas covered by JADES/GOODS-S (67.7 arcmin^2) and COSMOS/SMUVS (0.66 deg^2), we normalized the JADES/GOODS-S counts to match the COSMOS/SMUVS survey area, which is approximately 35 times larger than that of JADES/GOODS-S.

tense star formation activity (Navarro-Carrera et al. 2024a). The latter may explain why SB galaxies are less common at $\log_{10}(M_*/M_\odot) > 9$, now comprising only 26% of the population, with the remaining $\approx 10\%$ in the SFV region. Surprisingly, the fraction of SB galaxies primarily accumulates around $\log_{10}(M_*/M_\odot) \approx 9$ and strongly diminishes at higher stellar masses.

This result, indeed, indicates that the starburst phenomenon, at very high stellar masses (e.g., $M_* \gtrsim 10^{10} M_\odot$), likely requires galaxies to undergo either a major merger event (although the merger fraction is still not well constrained at high redshift), which could

trigger a violent episode of star formation activity (e.g., Cibinel et al. 2019; Renaud et al. 2022), or violent disk instabilities, gas accretion, and/or interactions (flybys and minor mergers) (e.g., Bournaud et al. 2012; Dannerbauer et al. 2017; Ho et al. 2019; Pan et al. 2019).

Interestingly, the results are independent on the assumed SFH. In addition to the initial assumptions discussed in §3.2, we explored also a delayed SFH with LEPHARE. Despite a different SFH, the trends illustrated in Figure 3 remain overall unchanged. Finally, by following Iani et al. (2024) (see their Appendix C), we investigated whether our results are influenced by the

introduction of a correction factor (k) to the UV-derived SFR adopted in this study. Specifically, we analyzed the theoretical evolution of the $\text{SFR}(\text{H}\alpha)/\text{SFR}(\text{UV})$ ratio as a function of time on a log-log scale, considering the prescriptions of Kennicutt (1998). This was done for the two metallicities used in our work, namely solar and sub-solar. We employed the same SFH models adopted for the SED fitting of our sources, including single burst and τ -models with τ values of 0.001, 0.01, 0.03, 1, 2, 3, 5, 8, 10, and 15 Gyr, along with a constant SFH model. These models incorporate the assumptions from the BPASS models (Eldridge & Stanway 2022), tailored for a Chabrier IMF, a cutoff mass of $100 M_{\odot}$, and excluding binary stars. By correcting the SFRs for galaxies younger than 15 Myr—where the UV estimates of SFR are known to be significantly underestimated (e.g., Kennicutt 1998; Calzetti 2013)—we observed that the overall sSFR distribution remains unaffected.

4.4. The emergence of the MS over cosmic time

We then inspected the emergence of the MS galaxies as a function of cosmic time. For this purpose, as we already assumed in Figure 2, we divided our sample into four different redshift bins, each spanning approximately 400 Myr: $z \approx 2.8 - 3.2$, $z \approx 3.2 - 3.9$, $z \approx 3.9 - 5$, and $z \approx 5 - 7$.

In Figure 4, we illustrate the sSFR distribution as a function of redshift, segmented into four stellar mass bins: we show 16 panels in total, with each row corresponding to a specific stellar mass bin and each column to a specific redshift bin.

As evident from Figure 4, there is a clear evolution of the SB/MS bimodality as a function of cosmic time. Going from the highest redshift bin ($z \approx 5 - 7$) to the lowest one ($z \approx 2.8 - 3.2$), the SB/MS bimodality evolves remarkably, showing that the onset of the MS over cosmic time clearly depends on the stellar mass regime considered.

Interestingly, as we move toward lower redshifts, SB galaxies become increasingly less common. Concurrently, we observe the onset of the “Main Sequence of star-forming galaxies”: for galaxies $M_{\star} \gtrsim 10^8 M_{\odot}$, the MS is already in place at $z \approx 5 - 7$ (more prominently for $M_{\star} \gtrsim 10^9 M_{\odot}$). Notably, MS galaxies are nearly absent in the lowest stellar mass regime, a trend consistent across all redshift bins.

This evolution over cosmic time suggests that at lower redshifts, the SB phenomenon becomes less common as galaxies have already assembled most of their M_{\star} . Significant events, such as major mergers, are thus required to trigger intense star formation episodes in massive galaxies. However, such events become increasingly rare

as we move toward lower redshifts ($z \lesssim 3$; e.g., Ventou et al. 2019, Puskás et al. in prep.).

This result is also in agreement with what has been presented in Bisigello et al. (2018), where they clearly observe that at $z \lesssim 3$ (see their Figure 8) the dominant mode of forming stars is the one that regulates the galaxies along the Main-Sequence, while SB galaxies are almost absent. Finally, in Figure 4, we also observe that within a fixed redshift bin, the SB/MS bimodality evolves as a function of stellar mass, as already shown in Figure 3.

The emergence of the “Main Sequence of star-forming galaxies” can be further observed in Figure 5, where we show the percentage evolution of MS, SB, and SFV galaxies across redshift and stellar mass bins. To estimate uncertainties in the percentages of MS, SB, and SFV galaxies, we employed Monte Carlo (MC) simulations following the approach used in Rinaldi et al. (2022). We generated 1000 mock catalogs from our initial dataset (JADES/GOODS-S + COSMOS/SMUVS), perturbing M_{\star} and SFR within their error bars for each simulation run. Subsequently, these mock galaxies were divided according to the same four stellar mass and redshift bins analyzed in Figure 5, adopting the criteria for MS, SB, and SFV classifications. Then, for each bin, we built up a distribution of the percentages for MS, SB, and SFV galaxies. We then determined the 1σ uncertainty as the half-distance between the 16th and 84th percentiles of each distribution. The errors were found to be up to a maximum of 5-6%.

Consistent with our analysis in Figures 3 and Figure 4, MS galaxies are almost absent at $\log_{10}(M_{\star}/M_{\odot}) \leq 9$. This may be due to either to the fact that very low-mass galaxies generally build up their M_{\star} through more violent episodes of star formation (e.g., Asada et al. 2024), or due to observational constraints that prevent the detection of such low-mass MS galaxies with correspondingly low SFR (below the threshold imposed by the current depth of our observations).

As we consider higher stellar masses ($\log_{10}(M_{\star}/M_{\odot}) > 9$), the Main Sequence starts taking place, becoming the dominant mode of forming stars at $\log_{10}(M_{\star}/M_{\odot}) > 9$ at $z \approx 3 - 7$. Figure 5 highlights again that the evolution of a galaxy along the MS is strictly correlated with M_{\star} . The onset of the MS becomes evident well before the Cosmic Noon ($z \approx 2$), particularly for galaxies with $M_{\star} > 10^9 M_{\odot}$, for which the MS is already in place by $z \approx 5 - 7$. This result suggests that galaxies can start evolving through secular processes well before the peak of Cosmic Star Formation, as suggested both in the past (e.g., Smit et al. 2016) and more recently (Langeroodi & Hjorth 2024). The transition from bursty to sec-

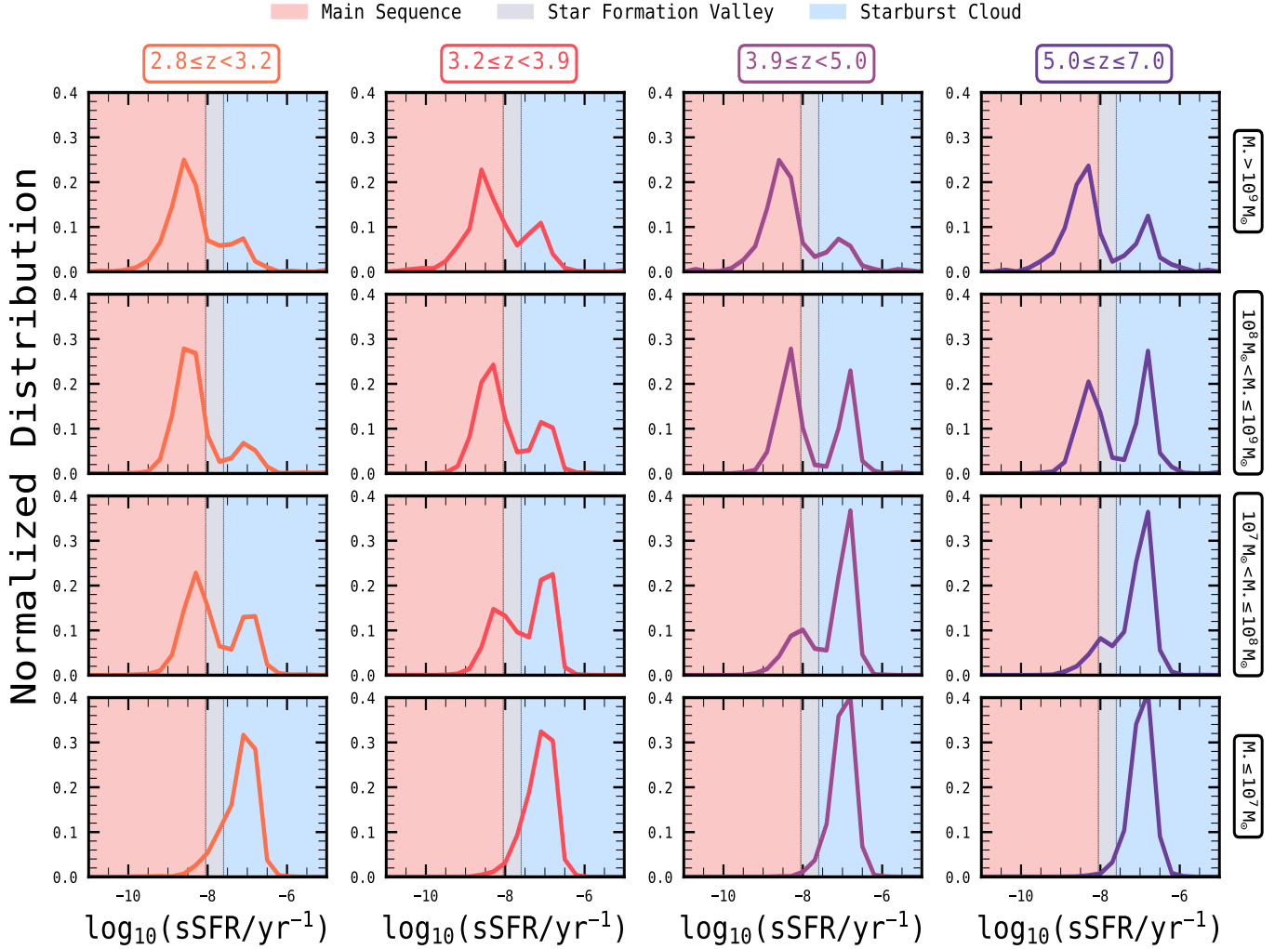


Figure 4. The sSFR distribution of the entire sample (JADES/GOODS-S + COSMOS/SMUVS) divided, this time, in four distinct stellar mass bins and four redshift bins. Each column refers to a specific redshift bin, while each row refers to a specific stellar mass bin. All 16 panels are color coded following Caputi et al. (2017): the star-formation MS for $\text{sSFR} > 10^{-8.05} \text{ yr}^{-1}$, the Starburst cloud for $\text{sSFR} > 10^{-7.60} \text{ yr}^{-1}$, and the Star Formation Valley for $10^{-8.05} \text{ yr}^{-1} \leq \text{sSFR} \leq 10^{-7.60} \text{ yr}^{-1}$. Also in this case, as we did in Figure 3, to consider the different areas covered by JADES/GOODS-S (67.7 arcmin^2) and COSMOS/SMUVS (0.66 deg^2), we normalized the JADES/GOODS-S counts to match the COSMOS/SMUVS survey area, which is approximately 35 times larger than that of JADES/GOODS-S.

ular star formation is especially evident in higher- M_* galaxies, which generally achieve a steady state of star formation at earlier epochs. This emphasizes that as galaxies build up their M_* , they increasingly favor secular evolution, because significant enhancements in their star formation activity typically require events like (minor and/or major) mergers or disk instabilities (e.g., Bournaud et al. 2012; Dannerbauer et al. 2017; Cibinel et al. 2019; Ho et al. 2019; Rodríguez Montero et al. 2019; Pan et al. 2019; Renaud et al. 2022). This implies that more massive galaxies are less likely to enter a SB phase without such significant events.

5. SUMMARY AND CONCLUSIONS

In this paper, we investigated the emergence of the “Main Sequence of star-forming galaxies” with M_* and redshift. For this purpose, we analyzed over 50,000 galaxies at $z \approx 3 - 7$ on the $\text{SFR} - M_*$ plane, spanning a wide stellar mass range $\log_{10}(M_*/M_\odot) \approx 6 - 11$. This study has been made possible thanks to the joint analysis of ultra-deep JWST data in GOODS-S (FRESCO, JADES, JEMS, and MIDIS), as well as shallower COSMOS/SMUVS data over an area $\approx 35\times$ larger, which allowed us to populate the high-mass end of the $\text{SFR} - M_*$ plane. This represents the first study that allows to reach very low stellar masses ($\log_{10}(M_*/M_\odot) < 7$) in blank fields without relying on gravitational lensing ef-

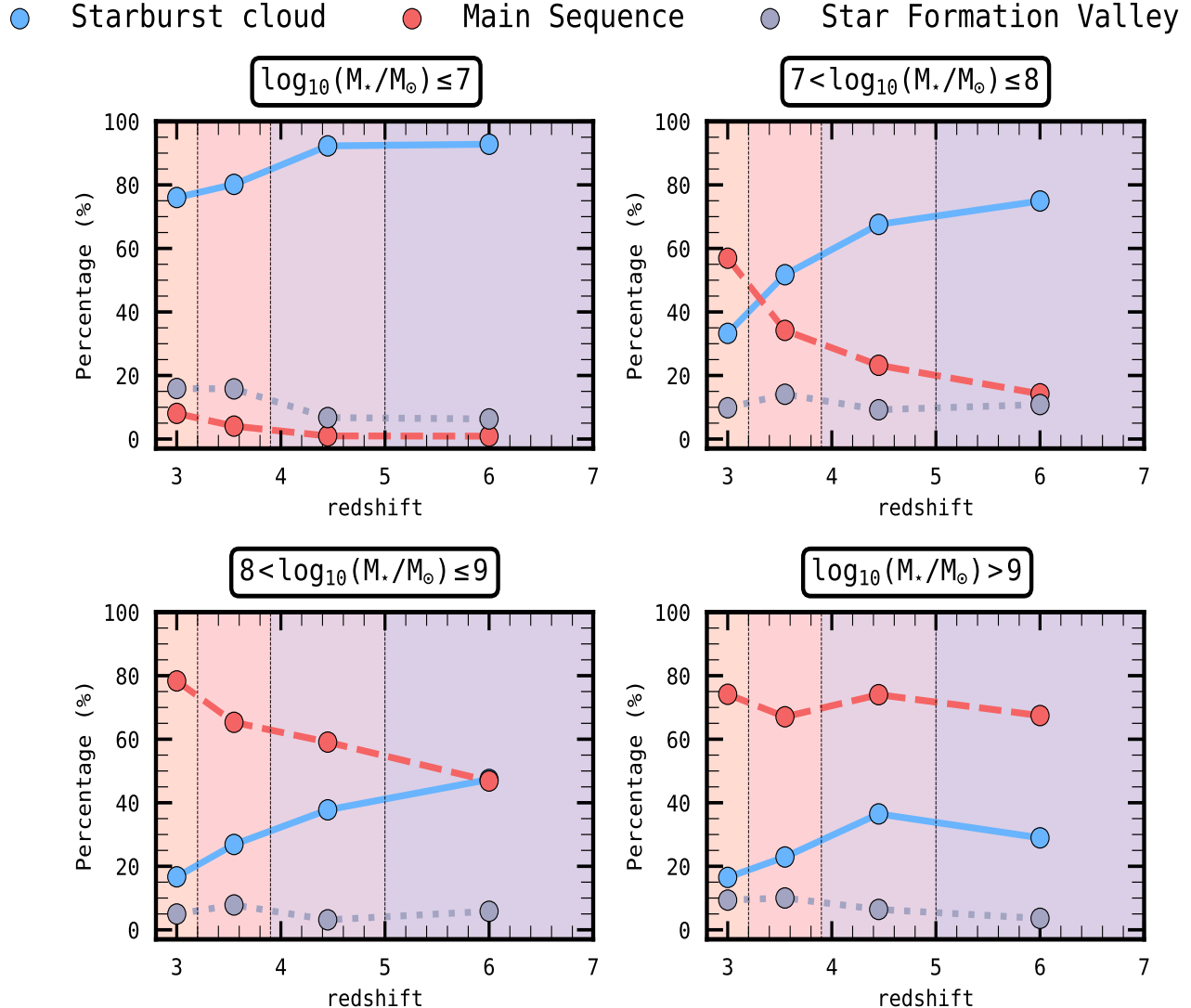


Figure 5. The evolution of the MS, SB, and SFV percentages with cosmic time in four stellar mass bins. Each panel has color bands corresponding to the four redshift bins analyzed in this study. Also in this case, to consider the different areas covered by JADES/GOODS-S (67.7 arcmin^2) and COSMOS/SMUVS (0.66 deg^2), we normalized the JADES/GOODS-S counts to match the COSMOS/SMUVS survey area, which is approximately 35 times larger than that of JADES/GOODS-S.

fects. We divided our sample into four redshift bins: $z \approx 2.8 - 3.2$, $z \approx 3.2 - 3.9$, $z \approx 3.9 - 5$, and $z \approx 5 - 7$. This division allowed us to probe similar amounts of time in each redshift bin ($\approx 400 \text{ Myr}$).

Our key findings are summarized as follows:

- In agreement with previous results (Caputi et al. 2017; Rinaldi et al. 2022), we find a bimodality on the $\text{SFR} - M_*$ plane, such that the vast majority of star-forming galaxies lie either on the MS or SB cloud. This pattern is clearly observed for all galaxies with $\log_{10}(M_*/M_\odot) > 7$ across all redshifts (Figure 2).
- Instead, at stellar masses $\log_{10}(M_*/M_\odot) < 7$, the two star-formation modes appear to converge in the $\text{SFR} - M_*$ plane (across all redshift bins), such that all low stellar-mass galaxies lie in the SB zone (Figure 3). Although our sample progressively loses completeness at such low stellar masses, we note that, at $z \approx 2.9 - 3.2$, it is still 50% complete down to $\log_{10}(M_*/M_\odot) \approx 6.3$, and 75% complete down to $\log_{10}(M_*/M_\odot) \approx 6.65$. Therefore, *this is not merely a selection effect*. Actually, this is expected on physical grounds. If the star formation is driven by the stochastic collapse of giant molecular clouds, a low M_* galaxy will by nature

be bursty. For example, a single minor gas accretion event could lead to the formation of $10^7 M_\odot$ in 10 Myr, doubling the stellar mass of a low-mass galaxy. Instead, for a high M_\star galaxy, a coordinated global SF event will be required to produce a SB (e.g., Gerola et al. 1980; Östlin et al. 2001; Atek et al. 2022). Deeper observations will be fundamental to further validate this finding.

- As the stellar mass increases, the MS of star-forming galaxies becomes more prominent and dominant, especially for $\log_{10}(M_\star/M_\odot) > 9$. Notably, at higher stellar masses ($\log_{10}(M_\star/M_\odot) \gtrsim 8$), the MS is already established by $z \gtrsim 4$. More importantly, for galaxies with $\log_{10}(M_\star/M_\odot) \gtrsim 9$, the MS is already in place at $z \approx 5 - 7$, aligning with the concept of galaxy downsizing (Sparre et al. 2015; Franco et al. 2020). In contrast, galaxies with lower stellar masses ($\log_{10}(M_\star/M_\odot) \lesssim 8$) at these redshifts ($z \approx 4 - 7$) are not yet on the MS and remain in the starburst phase (Figure 4). Thus, the emergence of the MS for star-forming galaxies at different redshifts heavily depends on M_\star (Figure 5), suggesting that galaxies with higher stellar mass can achieve a steady state well before the Cosmic Noon ($z \approx 2$; e.g., Smit et al. 2016; Langeroodi & Hjorth 2024).

In conclusion, current ultra-deep JWST observations indicate that very low-mass galaxies ($\lesssim 10^7 M_\odot$) predominantly experience bursty star formation, with only a few rare cases that can be classified as MS, typically showing signs of an evolved population. However, deeper observations will be crucial to confirm these findings. More importantly, our findings confirm that the emergence of the “Main Sequence of star-forming galaxies” in the SFR – M_\star plane is heavily M_\star dependent. The emergence of the “Main Sequence of star-forming galaxies” varies across cosmic time, with more massive galaxies ($M_\star \gtrsim 10^9 M_\odot$) establishing a more regulated, secular evolution already at $z \approx 5 - 7$. This highlights the critical role of M_\star in determining galaxy evolution.

Deeper and wider JWST observations will be instrumental in further constraining the emergence of the MS galaxies within the SFR – M_\star plane at different cosmic times.

The authors thank an anonymous referee for a careful reading and useful comments on this manuscript. The authors thank Nadav Peleg Brochstein and Daniil Ceban for useful discussion and tests on the effects of different SFHs on the stellar masses.

This work is based on observations made with the NASA/ESA/CSA JWST. The data were obtained from the Mikulski Archive for Space Telescopes (MAST) at the Space Telescope Science Institute, which is operated by the Association of Universities for Research in Astronomy, Inc., under NASA contract NAS 5-03127 for JWST. These observations are associated with JWST programs GTO #1180, GO #1210, GO #1963, GO #1895, and # 3215. The authors acknowledge the FRESCO, JEMS, and # 3215 teams led by coPIs P. Oesch, C. C. Williams, M. Maseda, D. Eisenstein, and R. Maiolino for developing their observing program with a zero-exclusive-access period. Processing for the JADES NIRCcam data release was performed on the lux cluster at the University of California, Santa Cruz, funded by NSF MRI grant AST 1828315. Also based on observations made with the NASA/ESA Hubble Space Telescope obtained from the Space Telescope Science Institute, which is operated by the Association of Universities for Research in Astronomy, Inc., under NASA contract NAS 526555. The data presented in this article were obtained from MAST at the Space Telescope Science Institute. The specific observations analyzed can be accessed via DOI: [10.17909/gdyc-7g80](https://doi.org/10.17909/gdyc-7g80), [10.17909/fsc4-dt61](https://doi.org/10.17909/fsc4-dt61), [10.17909/fsc4-dt61](https://doi.org/10.17909/fsc4-dt61), [10.17909/T91019](https://doi.org/10.17909/T91019), [10.17909/1rq3-8048](https://doi.org/10.17909/1rq3-8048), [10.17909/z2gw-mk31](https://doi.org/10.17909/z2gw-mk31).

K.I.C. and R.N.C. acknowledge funding from the Dutch Research Council (NWO) through the award of the Vici Grant VI.C.212.036. K.I.C. and E.I. acknowledge funding from the Netherlands Research School for Astronomy (NOVA). S.A. acknowledges support from the JWST Mid-Infrared Instrument (MIRI) Science Team Lead, grant 80NSSC18K0555, from NASA Goddard Space Flight Center to the University of Arizona.

This work was supported by research grants (VIL16599, VIL54489) from VILLUM FONDEN.

L.C. acknowledges support by grants PIB2021-127718NB-I00 and PID2022-139567NB-I00 from the Spanish Ministry of Science and Innovation/State Agency of Research MCIN/AEI/10.13039/501100011033 and by “ERDF A way of making Europe”.

J.A.M., and L.C., acknowledge support by grant PIB2021-127718NB-I00 from the Spanish Ministry of Science and Innovation/State Agency of Research MCIN/AEI/10.13039/501100011033 and by “ERDF A way of making Europe”.

L.C. thanks the support from the Cosmic Dawn Center received during visits to DAWN as international associate.

M.A. acknowledges financial support from Comunidad de Madrid under Atracción de Talento grant 2020-T2/TIC-19971.

Facilities: HST, JWST.

Software: ASTROPY (Astropy Collaboration et al. 2018), LEPHARE (Arnouts & Ilbert 2011), NUMPY (Harris et al. 2020), PANDAS (pandas development team 2020), PHOTUTILS (Bradley et al. 2021), SCIPY (Virtanen et al. 2020) SEXTRACTOR (Bertin & Arnouts 1996), TOPCAT (Taylor 2005).

REFERENCES

- Alberts, S., Williams, C. C., Helton, J. M., et al. 2024, *ApJ*, 975, 85
- Arnouts, S., & Ilbert, O. 2011, LePHARE: Photometric Analysis for Redshift Estimate, , ascl:1108.009
- Asada, Y., Sawicki, M., Abraham, R., et al. 2024, *MNRAS*, 527, 11372
- Ashby, M. L. N., Caputi, K. I., Cowley, W., et al. 2018, *ApJS*, 237, 39
- Astropy Collaboration, Price-Whelan, A. M., Sipőcz, B. M., et al. 2018, *AJ*, 156, 123
- Atek, H., Furtak, L. J., Oesch, P., et al. 2022, *MNRAS*, 511, 4464
- Atek, H., Richard, J., Kneib, J.-P., & Schaerer, D. 2018, *MNRAS*, 479, 5184
- Bacon, R., Brinchmann, J., Conseil, S., et al. 2023, *A&A*, 670, A4
- Bagley, M. B., Pirzkal, N., Finkelstein, S. L., et al. 2024, *ApJL*, 965, L6
- Bauer, A. E., Hopkins, A. M., Gunawardhana, M., et al. 2013, *MNRAS*, 434, 209
- Bertin, E., & Arnouts, S. 1996, *A&AS*, 117, 393
- Bhatawdekar, R., & Conselice, C. J. 2021, *ApJ*, 909, 144
- Bisigello, L., Caputi, K. I., Grogin, N., & Koekemoer, A. 2018, *A&A*, 609, A82
- Boogaard, L. A., Gillman, S., Melinder, J., et al. 2023, arXiv e-prints, arXiv:2308.16895
- Bournaud, F., Juneau, S., Le Floch, E., et al. 2012, *ApJ*, 757, 81
- Bouwens, R. J., Illingworth, G. D., Oesch, P. A., et al. 2015, *ApJ*, 803, 34
- Bouwens, R. J., Oesch, P. A., Stefanon, M., et al. 2021, *AJ*, 162, 47
- Bowler, R. A. A., Jarvis, M. J., Dunlop, J. S., et al. 2020, *MNRAS*, 493, 2059
- Bradley, L., Sipőcz, B., Robitaille, T., et al. 2021, astropy/photutils: 1.0.2, v1.0.2, Zenodo, doi:10.5281/zenodo.4453725
- Brammer, G. B., van Dokkum, P. G., & Coppi, P. 2008, *ApJ*, 686, 1503
- Brammer, G. B., van Dokkum, P. G., Franx, M., et al. 2012, *ApJS*, 200, 13
- Brinchmann, J., Charlot, S., White, S. D. M., et al. 2004, *MNRAS*, 351, 1151
- Bruzual, G., & Charlot, S. 2003, *MNRAS*, 344, 1000
- Bunker, A. J., Saxena, A., Cameron, A. J., et al. 2023, *A&A*, 677, A88
- Calabrò, A., Daddi, E., Fensch, J., et al. 2019, *A&A*, 632, A98
- Calzetti, D. 2013, in *Secular Evolution of Galaxies*, ed. J. Falcón-Barroso & J. H. Knapen, 419
- Calzetti, D., Armus, L., Bohlin, R. C., et al. 2000, *ApJ*, 533, 682
- Caputi, K. I., Deshmukh, S., Ashby, M. L. N., et al. 2017, *ApJ*, 849, 45
- Caputi, K. I., Caminha, G. B., Fujimoto, S., et al. 2021, *ApJ*, 908, 146
- Caputi, K. I., Rinaldi, P., Iani, E., et al. 2024, *ApJ*, 969, 159
- Casey, C. M., Berta, S., Béthermin, M., et al. 2012, *ApJ*, 761, 140
- Chabrier, G. 2003, *PASP*, 115, 763
- Cibinel, A., Daddi, E., Sargent, M. T., et al. 2019, *MNRAS*, 485, 5631
- Dannerbauer, H., Lehnert, M. D., Emonts, B., et al. 2017, *A&A*, 608, A48
- Deshmukh, S., Caputi, K. I., Ashby, M. L. N., et al. 2018, *ApJ*, 864, 166
- Eisenstein, D. J., Willott, C., Alberts, S., et al. 2023a, arXiv e-prints, arXiv:2306.02465
- Eisenstein, D. J., Johnson, B. D., Robertson, B., et al. 2023b, arXiv e-prints, arXiv:2310.12340
- Elbaz, D., Daddi, E., Le Borgne, D., et al. 2007, *A&A*, 468, 33
- Elbaz, D., Dickinson, M., Hwang, H. S., et al. 2011, *A&A*, 533, A119
- Eldridge, J. J., & Stanway, E. R. 2022, *ARA&A*, 60, 455
- Ellis, R. S., McLure, R. J., Dunlop, J. S., et al. 2013, *ApJL*, 763, L7
- Franco, M., Elbaz, D., Zhou, L., et al. 2020, *A&A*, 643, A30
- Galametz, A., Grazian, A., Fontana, A., et al. 2013, *ApJS*, 206, 10
- Gerola, H., Seiden, P. E., & Schulman, L. S. 1980, *ApJ*, 242, 517

- Green, G. 2018, *The Journal of Open Source Software*, 3, 695
- Guo, Y., Ferguson, H. C., Gialalisco, M., et al. 2013, *ApJS*, 207, 24
- Hainline, K. N., Johnson, B. D., Robertson, B., et al. 2024, *ApJ*, 964, 71
- Harris, C. R., Millman, K. J., van der Walt, S. J., et al. 2020, *Nature*, 585, 357.
<https://doi.org/10.1038/s41586-020-2649-2>
- Heckman, T. 2006, in *Encyclopedia of Astronomy and Astrophysics* (Murdin)
- Ho, S. H., Martin, C. L., & Turner, M. L. 2019, *ApJ*, 875, 54
- Iani, E., Caputi, K. I., Rinaldi, P., et al. 2024, *ApJ*, 963, 97
- Inoue, S., Dekel, A., Mandelker, N., et al. 2016, *MNRAS*, 456, 2052
- Iyer, K., Gawiser, E., Davé, R., et al. 2018, *ApJ*, 866, 120
- Jackson, T. M., Pasquali, A., Pacifici, C., et al. 2020, *MNRAS*, 497, 4262
- Kennicutt, Robert C., J. 1998, *ARA&A*, 36, 189
- Knapen, J. H., & James, P. A. 2009, *ApJ*, 698, 1437
- Koekemoer, A. M., Ellis, R. S., McLure, R. J., et al. 2013, *ApJS*, 209, 3
- Kron, R. G. 1980, *ApJS*, 43, 305
- Lamastra, A., Menci, N., Fiore, F., & Santini, P. 2013, *A&A*, 552, A44
- Langeroodi, D., & Hjorth, J. 2024, arXiv e-prints, arXiv:2404.13045
- Le Floch, E., Papovich, C., Dole, H., et al. 2005, *ApJ*, 632, 169
- Lee, N., Sheth, K., Scott, K. S., et al. 2017, *MNRAS*, 471, 2124
- Leitherer, C. 2001, in *Astronomical Society of the Pacific Conference Series*, Vol. 245, *Astrophysical Ages and Times Scales*, ed. T. von Hippel, C. Simpson, & N. Manset, 390
- Leitherer, C., Li, I. H., Calzetti, D., & Heckman, T. M. 2002, *ApJS*, 140, 303
- L’Huillier, B., Combes, F., & Semelin, B. 2012, *A&A*, 544, A68
- Li, Q., Conselice, C. J., Adams, N., et al. 2024, *MNRAS*, 531, 617
- Lyu, Y., Magnelli, B., Elbaz, D., et al. 2024, arXiv e-prints, arXiv:2406.11571
- Madau, P., & Dickinson, M. 2014, *ARA&A*, 52, 415
- Matthee, J., & Schaye, J. 2019, *MNRAS*, 484, 915
- McCracken, H. J., Milvang-Jensen, B., Dunlop, J., et al. 2012, *A&A*, 544, A156
- Mihos, J. C., & Hernquist, L. 1994, *ApJL*, 431, L9
- Muxlow, T., Beswick, R. J., Richards, A. M. S., & Thrall, H. J. 2006, in *Proceedings of the 8th European VLBI Network Symposium*, ed. W. Baan, R. Bachiller, R. Booth, P. Charlot, P. Diamond, M. Garrett, X. Hong, J. Jonas, A. Kus, F. Mantovani, A. Marecki, H. Olofsson, W. Schlueter, M. Tornikoski, N. Wang, & A. Zensus, 31
- Navarro-Carrera, R., Rinaldi, P., Caputi, K. I., et al. 2024a, arXiv e-prints, arXiv:2410.23249
- . 2024b, *ApJ*, 961, 207
- Noeske, K. G., Weiner, B. J., Faber, S. M., et al. 2007, *ApJL*, 660, L43
- Oesch, P. A., Bouwens, R. J., Illingworth, G. D., et al. 2014, *ApJ*, 786, 108
- Oesch, P. A., Brammer, G., Naidu, R. P., et al. 2023, *MNRAS*, 525, 2864
- Oke, J. B., & Gunn, J. E. 1983, *ApJ*, 266, 713
- Orlitova, I. 2020, arXiv e-prints, arXiv:2012.12378
- Östlin, G., Amram, P., Bergvall, N., et al. 2001, *A&A*, 374, 800
- Östlin, G., Pérez-González, P. G., Melinder, J., et al. 2024, arXiv e-prints, arXiv:2411.19686
- Pan, H.-A., Lin, L., Hsieh, B.-C., et al. 2019, *ApJ*, 881, 119
- pandas development team, T. 2020, *pandas-dev/pandas: Pandas, vlatest*, Zenodo, doi:10.5281/zenodo.3509134.
<https://doi.org/10.5281/zenodo.3509134>
- Pearson, W. J., Wang, L., Alpaslan, M., et al. 2019, *A&A*, 631, A51
- Peng, Y.-j., Lilly, S. J., Kovač, K., et al. 2010, *ApJ*, 721, 193
- Pérez-González, P. G., Costantin, L., Langeroodi, D., et al. 2023, *ApJL*, 951, L1
- Perrin, M. D., Sivaramakrishnan, A., Lajoie, C.-P., et al. 2014, in *Society of Photo-Optical Instrumentation Engineers (SPIE) Conference Series*, Vol. 9143, *Space Telescopes and Instrumentation 2014: Optical, Infrared, and Millimeter Wave*, ed. J. Oschmann, Jacobus M., M. Clampin, G. G. Fazio, & H. A. MacEwen, 91433X
- Popesso, P., Concas, A., Cresci, G., et al. 2023, *MNRAS*, 519, 1526
- Renaud, F., Bournaud, F., Agertz, O., et al. 2019, *A&A*, 625, A65
- Renaud, F., Segovia Otero, Á., & Agertz, O. 2022, *MNRAS*, 516, 4922
- Rinaldi, P., Caputi, K. I., van Mierlo, S. E., et al. 2022, *ApJ*, 930, 128
- Rinaldi, P., Caputi, K. I., Costantin, L., et al. 2023, *ApJ*, 952, 143
- Rinaldi, P., Caputi, K. I., Iani, E., et al. 2024, *ApJ*, 969, 12
- Rodighiero, G., Daddi, E., Baronchelli, I., et al. 2011, *ApJL*, 739, L40

- Rodríguez Montero, F., Davé, R., Wild, V., Anglés-Alcázar, D., & Narayanan, D. 2019, *MNRAS*, 490, 2139
- Romeo, A. B., & Fathi, K. 2016, *MNRAS*, 460, 2360
- Rosani, G., Caminha, G. B., Caputi, K. I., & Deshmukh, S. 2020, *A&A*, 633, A159
- Salmon, B., Papovich, C., Finkelstein, S. L., et al. 2015, *ApJ*, 799, 183
- Salpeter, E. E. 1955, *ApJ*, 121, 161
- Sánchez Almeida, J., Elmegreen, B. G., Muñoz-Tuñón, C., & Elmegreen, D. M. 2014, *A&A Rv*, 22, 71
- Santini, P., Fontana, A., Castellano, M., et al. 2017, *ApJ*, 847, 76
- Sargent, M. T., Béthermin, M., Daddi, E., & Elbaz, D. 2012, *ApJL*, 747, L31
- Schreiber, C., Pannella, M., Elbaz, D., et al. 2015, *A&A*, 575, A74
- Scoville, N., Aussel, H., Brusa, M., et al. 2007, *ApJS*, 172, 1
- Smit, R., Bouwens, R. J., Labbé, I., et al. 2016, *ApJ*, 833, 254
- Sonnett, S., Meech, K., Jedicke, R., et al. 2013, *PASP*, 125, 456
- Sparre, M., Hayward, C. C., Springel, V., et al. 2015, *MNRAS*, 447, 3548
- Speagle, J. S., Steinhardt, C. L., Capak, P. L., & Silverman, J. D. 2014, *ApJS*, 214, 15
- Stefanon, M., Labbé, I., Bouwens, R. J., et al. 2019, *ApJ*, 883, 99
- Tacchella, S., Dekel, A., Carollo, C. M., et al. 2016, *MNRAS*, 457, 2790
- Tadaki, K., Iono, D., Yun, M. S., et al. 2018, *Nature*, 560, 613
- Taniguchi, Y., Scoville, N., Murayama, T., et al. 2007, *ApJS*, 172, 9
- Taylor, M. B. 2005, in *Astronomical Society of the Pacific Conference Series*, Vol. 347, *Astronomical Data Analysis Software and Systems XIV*, ed. P. Shopbell, M. Britton, & R. Ebert, 29
- van Mierlo, S. E., Caputi, K. I., Ashby, M., et al. 2022, *A&A*, 666, A200
- Ventou, E., Contini, T., Bouché, N., et al. 2019, *A&A*, 631, A87
- Virtanen, P., Gommers, R., Oliphant, T. E., et al. 2020, *Nature Methods*, 17, 261
- Wang, E., Lilly, S. J., Pezzulli, G., & Matthee, J. 2019, *ApJ*, 877, 132
- Whitaker, K. E., van Dokkum, P. G., Brammer, G., & Franx, M. 2012, *ApJL*, 754, L29
- Whitaker, K. E., Franx, M., Leja, J., et al. 2014, *ApJ*, 795, 104
- Whitaker, K. E., Ashas, M., Illingworth, G., et al. 2019, *ApJS*, 244, 16
- Williams, C. C., Tacchella, S., Maseda, M. V., et al. 2023, *ApJS*, 268, 64
- Zhang, J., Li, Y., Leja, J., et al. 2023, *ApJ*, 952, 6